Applied Catalysis B: Environmental 205 (2017) 615–623

Contents lists available at ScienceDirect

Applied Catalysis B: Environmental

journal homepage: www.elsevier.com/locate/apcatb

$Bi_{24}O_{31}Br_{10}$ nanosheets with controllable thickness for visible–light–driven catalytic degradation of tetracycline hydrochloride

Chu-Ya Wang, Xing Zhang*, Hai-Bin Qiu, Gui-Xiang Huang, Han-Qing Yu*

CAS Key Laboratory of Urban Pollutant Conversion, Department of Chemistry, University of Science & Technology of China, Hefei 230026, China

ARTICLE INFO

Article history:
Received 8 November 2016
Received in revised form
30 December 2016
Accepted 4 January 2017
Available online 5 January 2017

Keywords:
Photocatalysis
$Bi_{24}O_{31}Br_{10}$ nanosheets
Thickness
Tetracycline hydrochloride
Visible light

ABSTRACT

Tetracycline hydrochloride (TTCH), a typical antibiotic, is widespread in aqueous environment, and its efficient and cost-effective removal is greatly desired. Among various physicochemical methods for TTCH degradation, visible-light-driven catalytic degradation is a promising one because of its utilization of solar energy. Bismuth oxybromide nanosheets have been found to be as efficient visible-light-driven photocatalysts, but the impact of thickness on their photocatalytic activity remains unclear. In this work, for the first time a series of thickness-controllable $Bi_{24}O_{31}Br_{10}$ nanosheets were synthesized without any surfactants, and their photocatlytic degradation of TTCH was explored. The photocatalytic degradation of TTCH was found to rely greatly on the generated free radicals and photogenerated h^+, which were formed by the photogenerated charge carriers. The experimental results clearly demonstrate that a decrease in thickness could enhance the separation and transportation efficiency of charge carriers and that the thinnest $Bi_{24}O_{31}Br_{10}$ nanosheets exhibited the best performance for photocatalytic TTCH degradation. Our findings might be helpful to expand the potential applications of bismuth oxybromide photocatalysts in water and wastewater treatment, and provide a new strategy for the modification of nanostructural photocatalysts.

1. Introduction

Tetracycline hydrochloride (TTCH) is a typical antibiotic commonly used in breeding industry and medical industry, and thus is widespread in aqueous environment. Because of its biotoxicity, TTCH is refractory to be degraded by traditional biological treatment processes [1–4]. Therefore, it is desired to find out an efficient and cost-effective physicochemical method to destruct its complex structure and remove its biotoxicity. Among various physicochemical methods, visible–light–driven photocatalytic degradation has been recognized as a promising approach because it is cost-effective, nontoxic, easily available and environmentally friendly [5–10].

Since the discovery of photocatalytic water splitting on a TiO_2 electrode in 1972, many other types of photocatalysts such as zinc oxide and bismuth oxyhalide (BiOX, X = Cl, Br or I) have been discovered, and these photocatalysts exhibit catalytic activities for pollutant degradation under ultraviolet or visible light irradiation [11–18]. It is widely recognized that the lattice defects greatly influence the catalytic efficiency. The defects on photocatalyst surface or in the shallow lattice of photocatalyst can efficiently trap photogenerated charge carriers and thus become active sites, while the defects in the bulk lattice prefer to act as a recombination center of h^+–e^- pairs and thus show a negative effect [19–21]. Thus, the maximization of surface and shallow lattice defects and minimization of bulk lattice defects are a robust way to enhance the efficiency of photocatalysts.

Since bismuth oxybromide with a special layered structure is recognized as a good photocatalyst, efforts have been made to enhance its photocatalytic activity, e.g., crystal facet selective exposure for the exposure of active sites, doping with other elements or oxygen–rich modification for the change of band structure, and heterojunction formation for the enhanced charge carrier separation efficiency [22–27]. The oxygen–rich modification for bismuth oxybromide has been reported previously. Some oxygen–rich bismuth oxybromide nanomaterials and heterojunctions, including $Bi_{24}O_{31}Br_{10}$ with three-dimensional morphology, $BiOBr/Bi_{24}O_{31}Br_{10}$ heterojunction, $Bi_{12}O_{17}Cl_2/Bi_{24}O_{31}Br_{10}$ heterojunction and $Bi_{24}O_{31}Cl_xBr_{10-x}$ solid solution, were synthesized. In

* Corresponding authors.
E-mail addresses: zhx0610@ustc.edu.cn (X. Zhang), hqyu@ustc.edu.cn (H.-Q. Yu).

http://dx.doi.org/10.1016/j.apcatb.2017.01.015
0926-3373/

these cases, cetyltrimethyl ammonium bromide (CTAB) was usually used as a Br resource and a surfactant [6,28–31]. However, so far little information is available about the impact of bismuth oxybromide thickness on the photocatalytic activity, and the mechanism of such an impact from the aspect of charge carrier remains unclear [17,32–34]. Furthermore, utilization of surfactant should be avoided because it is difficult for them to be removed from the surface of catalysts and thus to shield active sites [35].

In this work, a series of $Bi_{24}O_{31}Br_{10}$ nanosheets with different thicknesses were synthesized using a simple solvothermal route, and the thickness control was achieved without any surfactants for the first time. Then, their structural, physicochemical and electrochemical characteristics were examined. Also, the mechanism of the enhanced photocatalytic activity resulted from the decrease in thickness, in terms of band structure, charge carrier density, electron transfer and h^+-e^- separation efficiency, was investigated. In addition, a model to describe the visible–light–driven photocatalytic degradation process of TTCH over $Bi_{24}O_{31}Br_{10}$ nanosheets was established. With these results, the thickness-dependent photocatalytic activity and performance of the as-prepared $Bi_{24}O_{31}Br_{10}$ nanosheets for TTCH degradation were revealed and a new strategy for nanomaterial synthesis and modification as well as their applications in water and wastewater treatment was proposed.

2. Materials and methods

2.1. Synthesis of $Bi_{24}O_{31}Br_{10}$ nanosheets

All chemicals used in this work were analytical-grade reagents purchased from Shanghai Chemical Reagent Co., China, and used without further purification. In a typical synthesis procedure, 0.970 g $Bi(NO_3)_3 \cdot 5H_2O$ (2 mmol) was added into 10 mL ethylene glycol (EG). After 20-min vigorous stirring and sonication, the mixture was dispersed to form a homogeneous solution. Meanwhile, NH_4Br was added into 25-mL distilled water under vigorous stirring for 5–6 min to form a homogeneous solution in parallel. The dosage of NH_4Br was the key for the thickness control of $Bi_{24}O_{31}Br_{10}$ nanosheets, and they were 0.196 g (2 mmol) for the ultrathin nanosheets (noted as BOB-S), 0.979 g (10 mmol) for the middle thickness nanosheets (noted as BOB-M) and 1.959 g (20 mmol) for the thick nanosheets (noted as BOB-L), respectively. Then, the above two solutions were mixed with stirring, and a white suspension was formed immediately. Then, 1.2 mL ethanol amine was added into the above suspension dropwise and the suspension was kept stirring for 10 min to insure the perfect mixing of all these reactants. After that, all of these reactants were transferred into a 50-mL autoclave with Teflon linear, which was heated at 160 °C for 12 h, and then naturally cooled to ambient temperature. The resulting yellow solid powders were collected through centrifugation and washed with distilled water and alcohol for three times to remove the residual ions and organics. The product was then dried at 70 °C for 6 h prior to characterization.

2.2. Physicochemical characterization of the samples

The X–ray powder diffraction (XRD) patterns of the samples were obtained on a Philips X' Pert PRO SUPER diffractometer equipped with graphite monochromatized Cu Kα radiation (λ = 1.541874 Å). The scanning electron microscopy (SEM) images of the samples were taken with an X–650 scanning electron micro analyzer and a JSM–6700F field emission SEM (JEOL Co., Japan). The transmission electron microscopy (TEM) images of the samples were obtained on a TEM (JEM-2011, JEOL Co., Japan), using an electron kinetic energy of 200 kV. The high-resolution transmission electron microscopy (HRTEM) analysis was performed on an HRTEM (2010, JEOL Co., Japan) at an acceleration voltage of 200 kV. The chemical compositions and the valence states of constituent elements were determined by X-ray photoelectron spectroscopy (XPS) (ESCALAB250, Thermo Fisher Inc., USA). The diffuse reflectance spectra (DRS) were measured using a UV/Vis spectrophotometer (Solid 3700, Shimadzu Co., Japan). The electron spin resonance (ESR) (JES-FA200, JEOL Co., Japan) was used to detect bromine vacancies and reactive radicals. The surface area was measured by using the Brunauer-Emmett-Teller (BET) method with a Builder 4200 instrument (Tristar II 3020 M, Micromeritics Co., USA).

2.3. Electrochemical characterization

All electrochemical measurements were conducted with a homemade three–electrode system, with the as-prepared $Bi_{24}O_{31}Br_{10}$ nanosheets on glass carbon for electrochemical impedance spectroscopy (EIS) analysis and Mott–Schottky plots determination, or FTO conductive glass (photocurrent test) as the working electrode, Pt wire as the counter electrode and Ag/AgCl (KCl, 3 M) as the reference electrode. EIS analysis was conducted by applying an AC voltage amplitude of 5 mV within the frequency range from 10^6 to 10^{-2} Hz in 0.5 M $K_3[Fe(CN)_6]$ and $K_4[Fe(CN)_6]$ solution; Mott-Schottky plots were measured in 0.1 M Na_2SO_4 aqueous solution by impedance measurement at a fixed frequency of 1 kHz between the applied voltage range of 0–0.7 V; photocurrent response was determined in 0.1 M Na_2SO_4 aqueous solution by amperometric *i*–*t* curve measurement with a bias voltage of 0.28 V (the open-circuit voltage of as-prepared samples) for 650 s. All these measurements were performed using a computer-controlled potentiostat (CHI 660E, CH Instrument Co., China) with a three-electrode glass electrochemical cell. The light source used in photocurrent measurement was the same as that used in the photocatalytic measurements in the following section.

2.4. Photocatalytic performance evaluation

The photocatalytic activity of the $Bi_{24}O_{31}Br_{10}$ nanosheets for the degradation of TTCH was evaluated using a 500 W Xe arc lamp with a 420 nm cutoff filter as the light source at ambient temperature, and the radiation flux was fixed at 94 mW cm^{-2}. First, 10 mg of $Bi_{24}O_{31}Br_{10}$ nanosheets were added into 30-mL aqueous solution containing 20 mg L^{-1} TTCH, and stirred in dark for 60 min to ensure sufficient adsorption/desorption equilibrium. Then, the samples were collected at given time intervals under light irradiation and continuously magnetic stirring. TTCH concentration was measured using a high performance liquid chromatography (HPLC, 1260 Infinity, Agilent Co., USA) with an Agilent Eclipse XDB-C18 column (4.6 × 150 mm) and the column temperature of 30 °C. To measure the TTCH concentration, 60% acetonitrile and 40% deionized water (containing 0.1% formic acid) were used as the mobile phase at a flow rate of 1.0 mL min^{-1}, and the detection wavelength was 273 nm. A liquid chromatography-mass spectrometry (LC–MS) (6460 LC/QQQ, Agilent Co., USA) was used to determine the intermediate products from TTCH degradation. The total organic carbon (TOC) concentration was measured using a TOC analyzer (Muti N/C 2100, Analytik Jena AG, Germany).

3. Results and discussion

3.1. Structural, morphological and chemical characteristics of $Bi_{24}O_{31}Br_{10}$ nanosheets

The morphology of the as-prepared products was observed using SEM and TEM (Fig. 1). The SEM images show that all these three samples possessed large-scale 2D sheet-like structures and the size of these nanosheets were about 0.5–1.0 μm, indicating

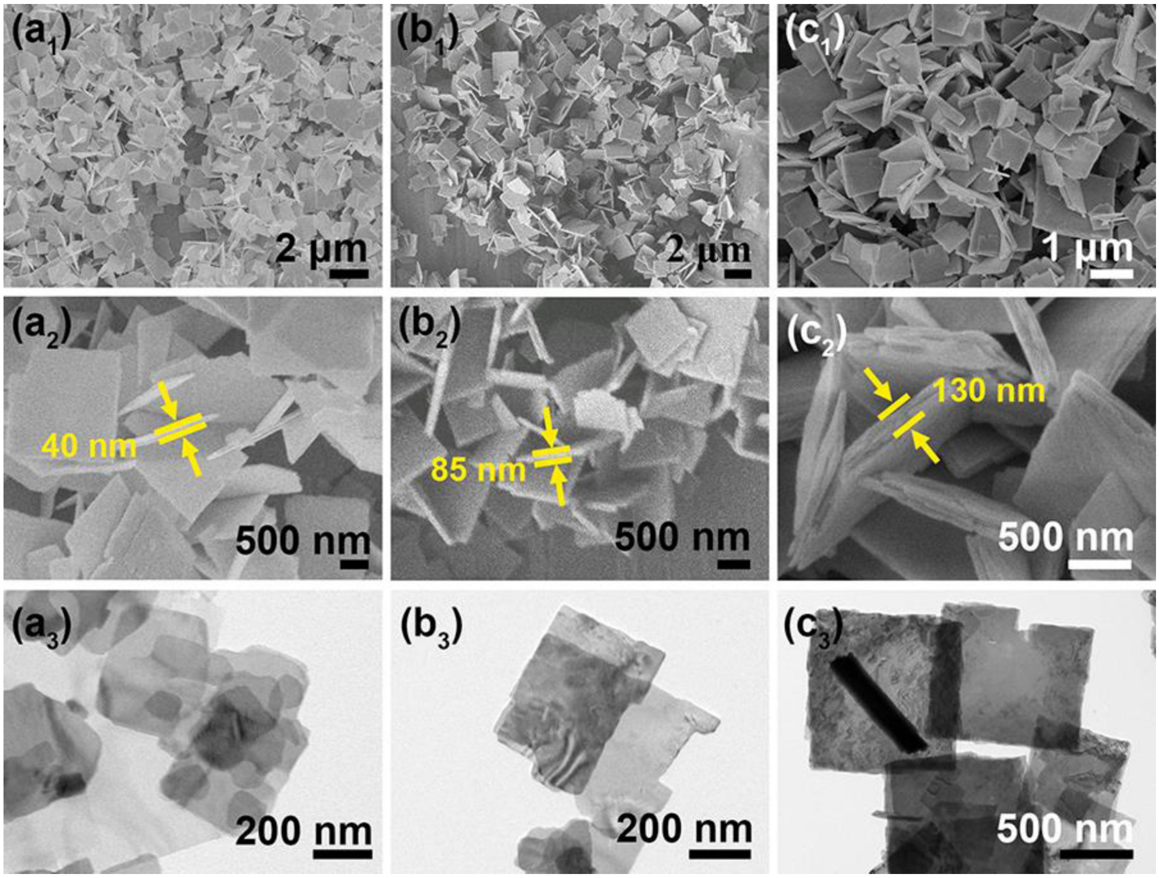

Fig. 1. (a1)–(c1) Low magnification and (a2)–(c2) high magnification SEM images, and (a3)–(c3) TEM images of BOB-S, BOB-M and BOB-L.

that theses nanomaterials exhibited a well uniformed morphology. However, the thicknesses of the three samples were different, which were further measured using TEM. The TEM images further confirm that these samples had 2D sheet-like structures. Their thicknesses are shown in Fig. 1a_2–c_2. The three samples with different thicknesses were noted as BOB-S for ~40 nm, BOB-M for ~85 nm and BOB-L for ~130 nm, respectively. The thickness distribution of BOB-S, BOB-M and BOB-L is shown in Fig. S1. In a typical solvothermal process, the crystal growth of the $Bi_{24}O_{31}Br_{10}$ nanosheets is supposed to be an Ostwald ripening process [20]. The size of bismuth oxyhalide nanocrystals can be controlled by changing the size of micelles [36]. When the concentration of Br^- in the solution decreased, the size of micelles became smaller, and thus the thickness of nanosheets decreased correspondingly. In addition, with a decrease in thickness, fragmentation occurred on the edge of the nanosheets, indicating that the decrease in thickness weakened the mechanical strength of the nanosheets, thus resulting in the crystallinity decrease of BOB-S.

The matter phases and the crystal structures of the products were verified with the powder XRD results (Fig. 2). All the diffraction peaks could be indexed to $Bi_{24}O_{31}Br_{10}$ with the lattice parameters of a = 1.0130, b = 0.4008 and c = 2.9970 nm (JCPDS card No. 75-0888). No peaks of any other phases were observed, indicating the purity of the three samples. The strong and sharp reflection peaks suggest that the as-prepared samples were well crystallized. In addition, the peaks in the XRD pattern of BOB-S, especially the peaks at 10.520, 31.823 and 39.834°, were slightly wider than those of BOB-M and BOB-L. This result implies that the decrease in crystallinity occurred for BOB-S, which is in accordance with the TEM images.

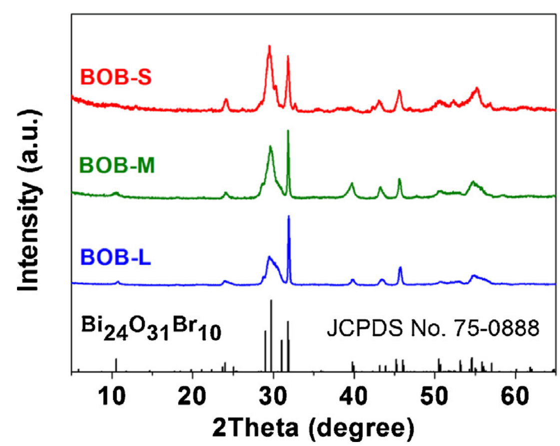

Fig. 2. XRD patterns of BOB-S, BOB-M and BOB-L.

The structure of BOB-S was further characterized using an HRTEM. The square shaped BOB-S nanosheets with fragmented edges and tortuous surface showed the ultrathin 2D-sheet-like morphology and the existence of lattice defects (Fig. 3a). Fig. 3b, which was taken from the edge of a single nanosheet noted in Fig. 3a, reveals a high crystallinity and clear lattice fringes. The continuous lattice fringes with an interplanar lattice spacing of 0.30 nm, as marked in Fig. 3b, matched well with the $(21\overline{3})$ atomic planes of $Bi_{24}O_{31}Br_{10}$, whose diffraction peak in XRD occurred at 29.76° (Fig. 2). Moreover, the STEM and EDS mapping results show that the three elements, Bi, O and Br, possessed a uniform distribution (Fig. 3c). The integrated EDS spectrum (Fig. S2) shows that only Bi, O and Br were detected and no other elements were found

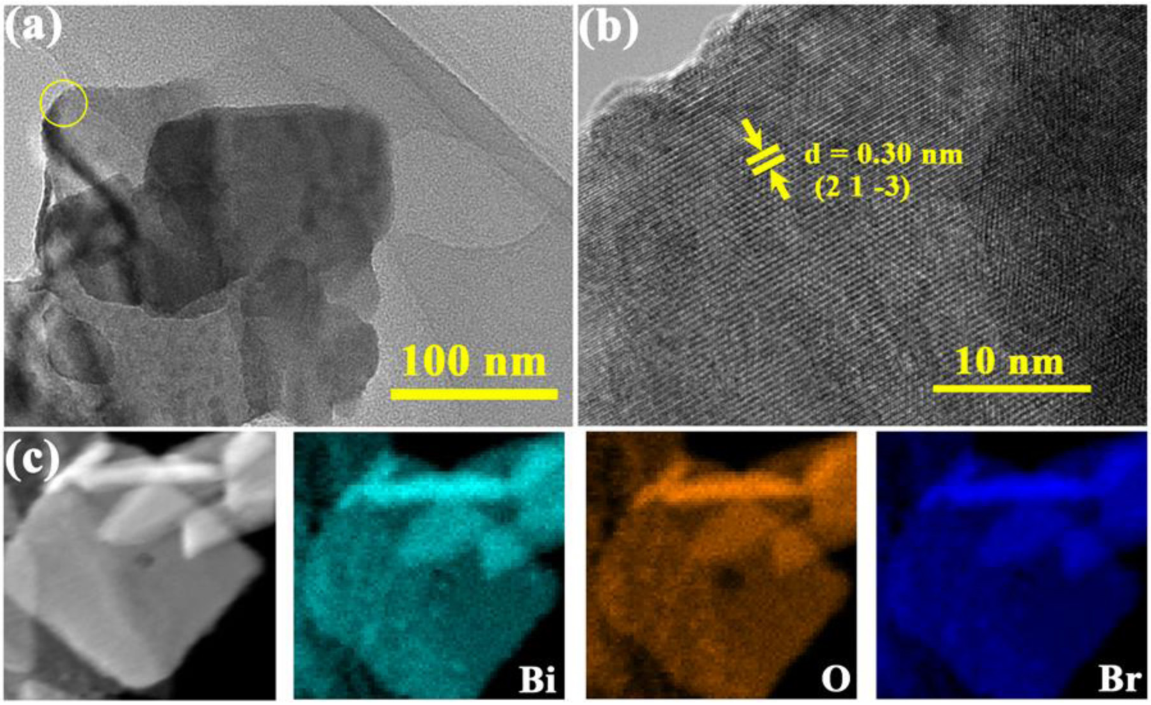

Fig. 3. (a) TEM image, (b) HRTEM image, and (c) STEM image and EDS mapping of BOB-S.

in BOB-S. The atomic percentage contents of Bi, O and Br calculated from the integrated EDS spectrum result were 40.1, 50.8 and 9.1%, respectively. Compared to the theoretical values of 36.9, 47.7 and 15.4% for Bi, O and Br, respectively, the atomic percentage contents of Bi and O both increased by about 3%, while that of Br decreased by about 6%. This result indicates the existence of bromine vacancies in the crystal of BOB-S, which was the main lattice defect responsible for the crystallinity decrease as reflected by the XRD patterns. The bromine vacancies in these three samples were confirmed by the ESR results (Fig. S3). Therefore, BOB-S possessed the highest ratio of surface and shallow lattice bromine vacancies, because the intensities of bromine vacancies signals of these three samples were of a similar level and BOB-S was the thinnest one.

A UV–vis spectrophotometer was used to examine the optical properties of BOB-S, BOB-M and BOB-L, and the resulted DRS are shown in Fig. S4a. Each sample had a similar typical band edge absorption around 500 nm. Their absorption edges around 500 nm were perfectly parallel and very close to each other, indicating that there were no obvious differences among their band gap energy.

The band gap of a semiconductor can be deduced from the equation below:

$$\alpha(h\nu) = A(h\nu - E_g)^{n/2} \tag{1}$$

where α, $h\nu$, E_g, and A are the absorption coefficient, photon energy, band gap, and a constant, respectively. n in this equation depends on the characteristics of the transition in a semiconductor. For BiOX (X = Cl, Br or I), its value is 4 for its indirect transition.

The Tauc plots of BOB-S, BOB-M and BOB-L are shown in Fig. S4b, which were calculated based on the results of UV–vis DRS. The semiconductor band gap is usually governed by the linear Tauc region, which is just above the optical absorption edge [37]. The specific band gap energies of BOB-S, BOB-M and BOB-L were 2.30, 2.33 and 2.35 eV, respectively. Such a similarity in their band gap energies was in correspondence with the absorption edge result in UV–vis DRS.

The XPS analysis was performed to explore the surface composition and the chemical state of the as-prepared catalyst samples. From the full scan spectrum, the peaks of the Bi, O, Br, and C elements could be identified (Fig. 4a). The XPS spectra were corrected for specimen charging by referencing the C 1s peak to 284.60 eV. The Bi 4f XPS spectra in Fig. 4c show two main peaks with the splitting energy Δ = 5.4 eV, corresponding to the Bi $4f_{7/2}$ and Bi $4f_{5/2}$ of Bi^{3+}, respectively. The O 1s core level spectra in Fig. 4d fit well with the peak at 529.4 eV, which belongs to O^{2-} from a bismuth-oxygen bond in $Bi_{24}O_{31}Br_{10}$ nanosheets. The Br 3d XPS spectra in Fig. 4e exhibit two main peaks with binding energies at 67.9 and 69.4 eV, corresponding to Br $3d_{5/2}$ and Br $3d_{3/2}$ of Br^-, respectively. It is worth noting that the Br 3d peaks of BOB-S exhibit a right–shift by about 0.4 eV, which was caused by the decrease in the atomic percentage content of Br. The highest ratio of surface and shallow lattice bromine vacancies led to the presence of more oxygen atoms in BOB-S crystal in order to achieve the charge balance. Since the electronegativity of O was much higher than that of Br, more O in BOB-S crystal would decrease the electron density on Br. Thus, the binding energy of Br 3d increased and finally the peaks of Br 3d in the XPS spectra occurred at a position corresponding to a higher energy. Therefore, the right–shift of Br 3d peaks in BOB-S indicates the existence of bromine vacancies as the lattice defects, which is in accordance with the integrated EDS spectrum result. Additionally, the valence band (VB) of BOB-S, BOB-M and BOB-L were measured qualitatively by XPS VB spectra (Fig. 4b). The VB top potential energy of BOB-S was much higher than those of BOB-M and BOB-L, which was caused by the bromine vacancies in BOB-S crystal, suggesting that BOB-S might exhibit a higher catalytic activity under visible light irradiation.

3.2. Band structures and photoelectrical properties of $Bi_{24}O_{31}Br_{10}$ nanosheets

Band structure and charge carrier are the two key factors governing the photocatalytic activity of a semiconductor nanomaterial. To prole the relative band structures of the as-prepared catalyst samples, the flat-band potential was measured using the electrochemical method, and the resulted Mott-Schottky plots are

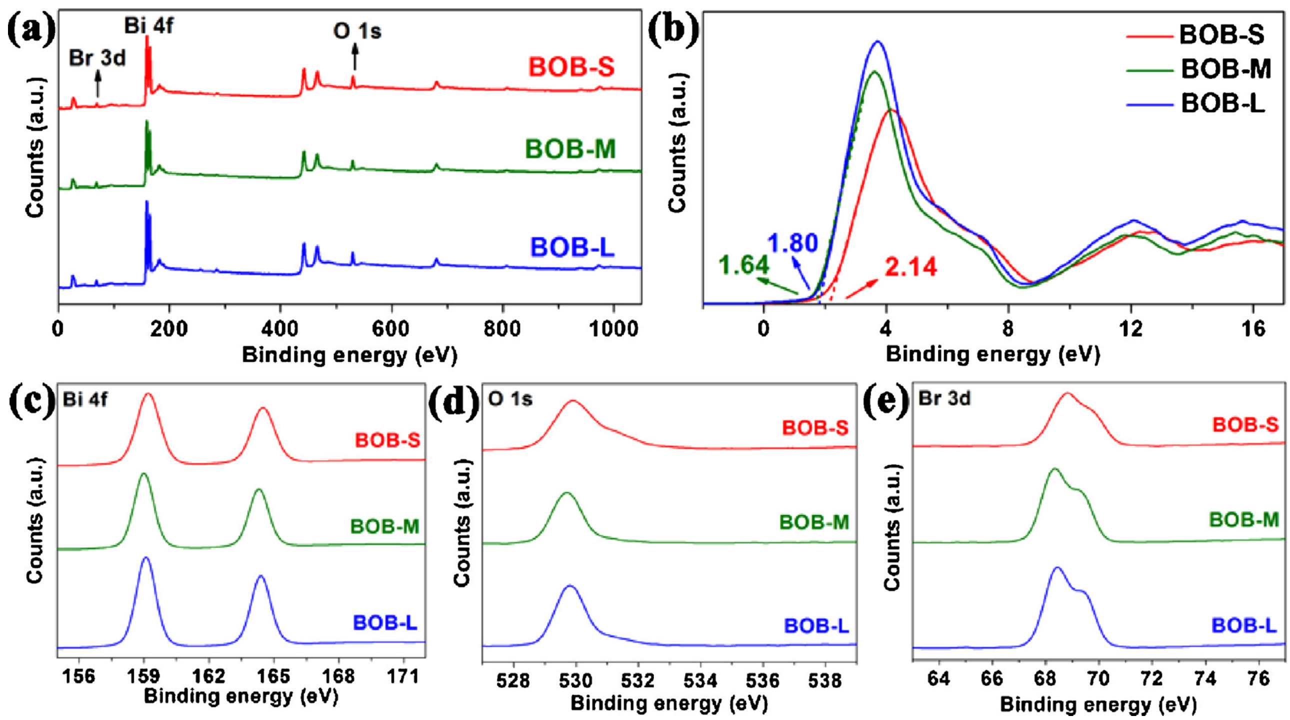

Fig. 4. (a) XPS survey spectra, (b) valence band spectra, (c) Bi 4f, (d) O 1s, and (e) Br 3d spectra of BOB-S, BOB-M and BOB-L.

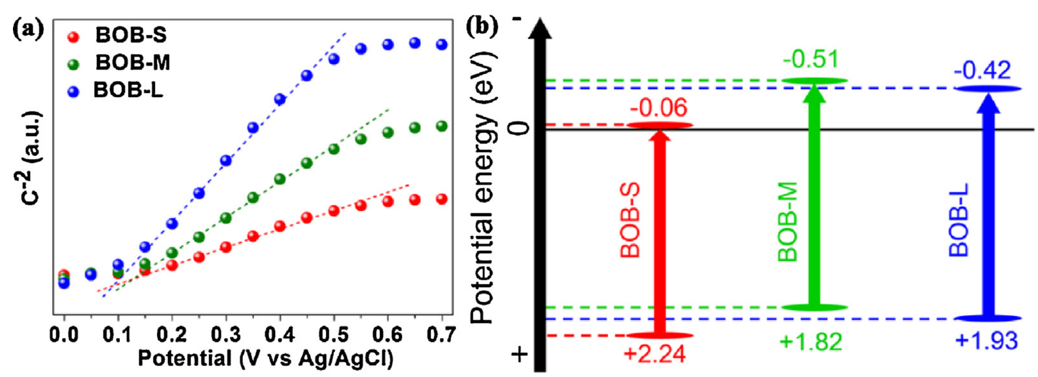

Fig. 5. (a) Mott-Schottky plots, and (b) band energy diagrams of BOB-S, BOB-M and BOB-L.

shown in Fig. 5a. The Mott-Schottky plots of all these samples possess a positive slope, which is typical for n-type semiconductors, indicating that the charge carriers in these nanomaterials were photogenerated e^-. From the Mott-Schottky plots, the conduction band (CB) bottom potential energies of BOB-S, BOB-M and BOB-L were calculated as −0.06, −0.51 and −0.42 eV, respectively. Thus, the VB top potential energy of BOB-S, BOB-M and BOB-L were calculated to be 2.24, 1.82 and 1.93 eV, respectively (from $E_{VB} = E_g + E_{CB}$), as shown in Fig. 5b. The VB top of BOB-S down-shifted by 0.42 and 0.31 eV compared with BOB-M and BOB-L, respectively, suggesting that the oxidation activity of photogenerated h^+ in BOB-S was higher than those of BOB-M and BOB-L.

In the Mott-Schottky plots in Fig. 5a, the slopes of the liner part suggest the charge carrier density information of the catalyst samples. The charge carrier density (N_d) can be calculated from the slope of Mott–Schottky plots with the following equation:

$$N_d = (2/e_0\varepsilon\varepsilon_0)[d(C^{-2})/dV]^{-1} \quad (2)$$

where e_0 is the electron charge, ε is the dielectric constant of the sample, ε_0 is the permittivity of the vacuum, and $d(c^{-2})/dV$ is the slope of the liner part in the Mott–Schottky plots, meaning that the charge carrier density is reciprocal with the slope.

The charge carrier density of BOB-S was 1.94 and 3.22 times higher than those of BOB-M and BOB-L, respectively, indicating that more active species could be generated over BOB-S and it might exhibit a higher photocatalytic activity than BOB-M and BOB-L.

In addition to band structure and charge carrier, the charge transfer and the recombination of h^+-e^- pairs also have impacts on the photocatalytic activity of catalysts. Thus, EIS analysis and photocurrent tests of BOB-S, BOB-M and BOB-L were performed and the results are shown in Fig. 6. The highest charge transfer efficiency of BOB-S was confirmed by the smallest curvature radius in the EIS Nyquist spectra (Fig. 6a). The calculated impedances of BOB-M and BOB-L were 3.11 and 4.79 times higher than that of BOB-S, indicating that the admittance of BOB-S was 3.11 and 4.79 times higher than those of BOB-M and BOB-L, respectively.

Moreover, the highest photocurrent response of BOB-S also indicates its greatest charge carrier density and the most efficient charge transfer (Fig. 6b). The photocurrent response of BOB-S, which is in proportion to the charge carrier density and is in inverse proportion to the impedance, was calculated to be 2.95 and

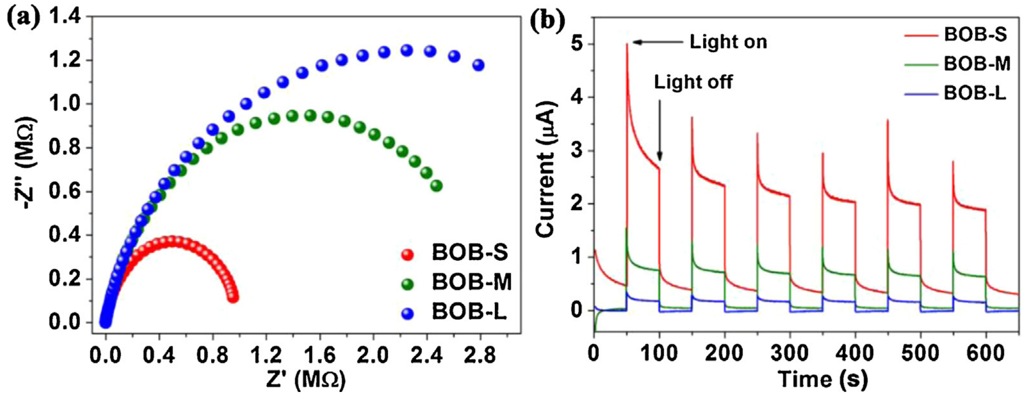

Fig. 6. (a) EIS Nyquist spectra, and (b) photocurrent responses of BOB-S, BOB-M and BOB-L.

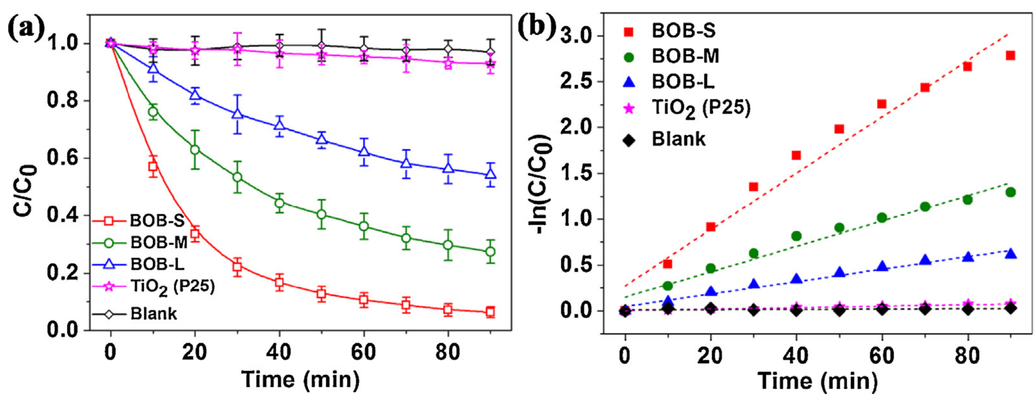

Fig. 7. (a) Photocatalytic degradation curves, and (b) kinetic curves of BOB-S, BOB-M, BOB-L, TiO_2 (P25) and blank test.

10.31 times higher than those of BOB-M and BOB-L, respectively. Thus, since the charge carrier density of BOB-S was 1.94 and 3.22 times higher than those of BOB-M and BOB-L and the influence of impedance was offset by the applied bias voltage, the h^+–e^- separation efficiency of BOB-S was 1.52 and 3.20 times higher than those of BOB-M and BOB-L, respectively. The defects on the surface or in the shallow lattice can efficiently trap the photogenerated e^- and thus play a positive role in h^+-e^- separation, while the defects in the bulk lattice prefer to act as the recombination center of h^+-e^- pairs and thus show a negative effect [20]. These results reveal that BOB-S exhibited the best performance in terms of charge carrier density, h^+-e^- separation and charge transportation, implying the better photocatalytic performance of BOB-S than BOB-M and BOB-L, which was attributed to its ultrathin thickness.

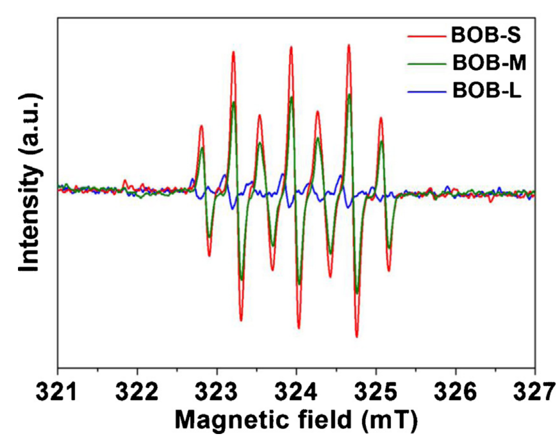

Fig. 8. ESR signals of •OOH produced by BOB-S, BOB-M and BOB-L.

3.3. Photocatalytic degradation of TTCH by $Bi_{24}O_{31}Br_{10}$ nanosheets

To explore the feasibility of using the $Bi_{24}O_{31}Br_{10}$ nanosheets for water and wastewater treatment, degradation of TTCH by the prepared catalysts and TiO_2 (P25) under visible light irradiation was tested, and the results are shown in Fig. 7a. TTCH was sable under visible light irradiation in the absence of photocatalysts. Only less than 10% of TTCH was degraded by TiO_2, indicating that the photocatalytic degradation of TTCH by TiO_2 (P25) under visible light irradiation was very limited. However, the three samples performed much better than TiO_2. BOB-S had the best TTCH degradation performance of and more than 95% of TTCH was degraded within 90 min, while about 70% and 45% of TTCH were degraded by BOB-M and BOB-L, respectively. In addition to the high photocatalytic activity, BOB-S also exhibited good stability and reusability (Fig. S5 and S6), both of which are essential for the practical applications.

The photocatalytic activities of the three catalysts were further compared through calculating their kinetic constants. The degradation kinetics of TTCH was obtained by fitting the experimental data to the Langmuir–Hinshelwood model. Since the reactant concentration was low, the following pseudo first-order kinetics equation was used:

$$-\ln(C_t/C_0) = kt \tag{3}$$

where C is TTCH concentration and k is the apparent rate constant. The reaction kinetics of the samples could be fitted well by the pseudo first-order rate model with high correlation coefficients

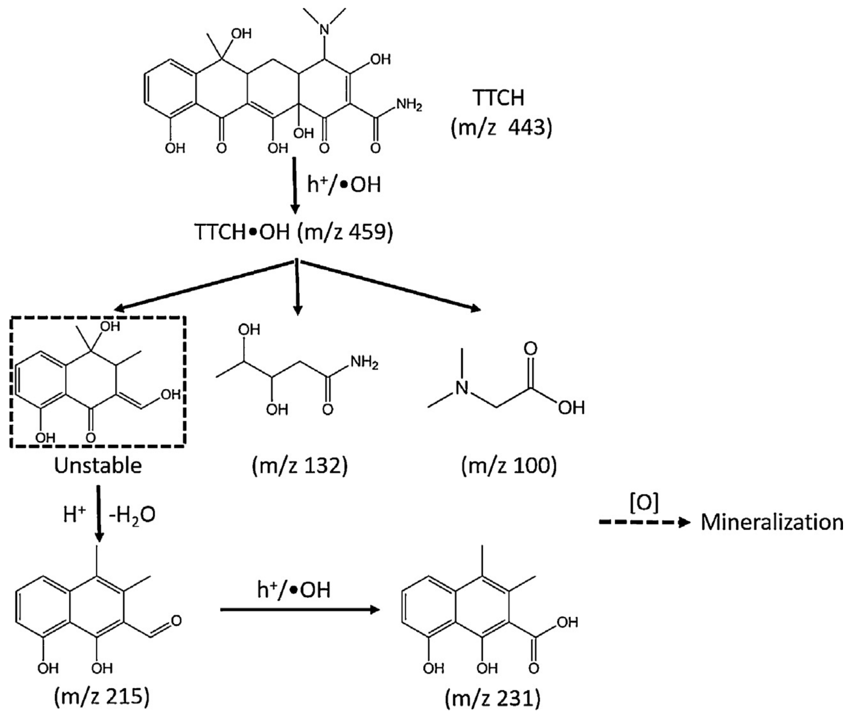

Fig. 9. Proposed photocatalytic degradation pathway of TTCH by BOB-S.

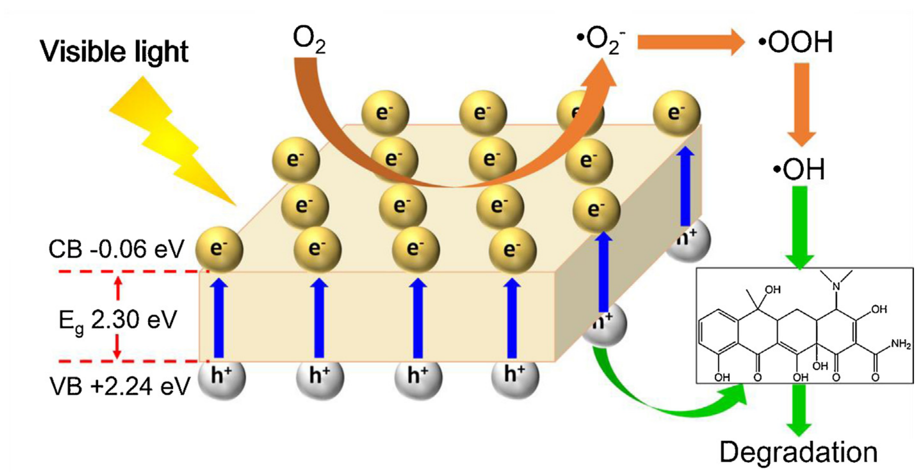

Fig. 10. Schematic of photocatalytic TTCH degradation over BOB-S.

(more than 0.96), which is shown in Fig. 7b. The calculated *k* values were 0.031, 0.014 and 0.007 min^{-1} for BOB-S, BOB-M and BOB-L, respectively.

In order to investigate the impact of the surface area on the TTCH degradation, the BET surface areas of the three catalysts were measured, and those of BOB-S, BOB-M and BOB-L were 8.571, 9.710 and 6.100 $m^2\,g^1$, respectively (Fig. S7). The surface-area-normalized photocatalytic activity of BOB-S (3.62 $mg\,min^{-1}\,m^{-2}$) was substantially higher than those of BOB-M (1.44 $mg\,min^{-1}\,m^{-2}$) and BOB-L (1.15 $mg\,min^{-1}\,m^{-2}$), indicating that the highest photocatalytic activity of BOB-S should not be attributed to its surface area.

In the photocatalytic degradation process, the generated free radicals are usually the active species, including superoxide radical ($^{\bullet}O_2^-$) and hydroxyl radical ($^{\bullet}OH$). To investigate the generation of $^{\bullet}O_2^-$ and $^{\bullet}OH$ over the three catalysts, nitroblue tetrazolium (NBT) and terephthalic acid (TPA) were respectively chosen to trap the $^{\bullet}O_2^-$ and $^{\bullet}OH$ generated in the visible light irradiation, and the results are shown in Fig. S8. When $^{\bullet}O_2^-$ was trapped by NBT, the characteristic peak of NBT at 260 nm in the UV–vis absorption spectrum decreased, and the specific value of the peak decrease was in proportion to the $^{\bullet}O_2^-$ concentration. Similarly, the characteristic peak of TPA$^{\bullet}$OH at 317 nm in the fluorescence spectrum increased when TPA reacted with $^{\bullet}OH$ to form TPA$^{\bullet}$OH, and the specific value of the peak increase was in proportion to the $^{\bullet}OH$ concentration. Thus, the generated $^{\bullet}O_2^-$ over BOB-S was calculated to be 1.6 and 5.4 times higher than those for BOB-M and BOB-L, respectively. For the generated $^{\bullet}OH$ by BOB-S was 1.43 and 5.11 times higher than those by BOB-M and BOB-L, respectively.

In visible light irradiation process, $^{\bullet}O_2^-$ could also be transformed into $^{\bullet}OH$ via series of radical reactions. A typical intermediate, $^{\bullet}OOH$, was detected in the ESR test, and the results are shown in Fig. 8. The seven peaks with the intensity of 1:2:1:2:1:2:1 are the characteristic peaks of $^{\bullet}OOH$, and the peak intensity is in

proportion to the concentration of $^\bullet$OOH [35,38]. The generated $^\bullet$OOH by BOB-S was calculated to be 1.4 and 5.2 times higher those by BOB-M and BOB-L, respectively, which is in correspondence with the $^\bullet O_2^-$ and $^\bullet$OH results. Thus, the generated $^\bullet O_2^-$ could be transformed into $^\bullet$OH in our system via the following reactions:

$$O_2 + e^- \rightarrow {}^\bullet O_2^- \quad (4)$$

$$^\bullet O_2^- + H_2O \rightarrow {}^\bullet OOH + OH- \quad (5)$$

$$^\bullet OOH + H_2O + 2e^- \rightarrow {}^\bullet OH + 2OH^- \quad (6)$$

3.4. Photocatalytic TTCH degradation mechanisms over BOB-S

The photocatalytic degradation of organic pollutants usually occurs through the oxidation by $^\bullet$OH, $^\bullet O_2^-$ or h^+ [39,40]. To reveal the roles of the active species responsible for the TTCH degradation under visible light irradiation, we performed series experiments by adding various scavengers. The applied scavengers in these investigations included sodium oxalate ($Na_2C_2O_4$) for h^+, *tert*-butyl alcohol (TBA) for $^\bullet$OH, *p*-benzoquinone (PBQ) for $^\bullet O_2^-$ and N_2–purging for molecular oxygen [37,41–43]. The TTCH degradation was greatly suppressed by the adding of $Na_2C_2O_4$ (Fig. S9), and non-negligible suppression also occurred when PBQ, N_2–purging and TBA were used, indicating that the contribution of the active species on the TTCH removal was in the order of $h^+ > {}^\bullet O_2^- > {}^\bullet OH$. Thus, the as-prepared BOB–S sample with the highest VB top potential energy and the most free radicals possessed the best performance of TTCH degradation.

LC–MS was used to analyze the intermediates formed in the photocatalytic degradation process of TTCH and five intermediates were detected (Fig. S10). The product ion at *m*/*z* 459 was the hydroxylated product of TTCH (noted as TTCH$^\bullet$OH), implying that the excitation of TTCH might be the first step of degradation. Then, the carbon chain of TTCH$^\bullet$OH was split into several parts, which were detected as the product ions at *m*/*z* 132, 100 and 215. However, the intermediate *m*/*z* 215 was transformed from an unstable intermediate, which was another substance formed from the direct split of TTCH$^\bullet$OH. When the reactions progressed, the concentration of the intermediate *m*/*z* 215 remained stable, while the concentration of the intermediate *m*/*z* 231 was very low at the beginning but increased rapidly in the TTCH degradation process, suggesting that the intermediate *m*/*z* 215 was transformed into the intermediate *m*/*z* 231. The destruction of TTCH resulted in the loss of biotoxicity and the degradation intermediates could be further degraded using a microbial degrdation process [1]. Furthermore, more than 20% of total organic carbon was removed within 120-min visible light irradiation (Fig. S11). Since BOB-S possessed a high $^\bullet$OH-generating activity and TTCH could be effectively degraded by $^\bullet$OH, the remaining TOC could be finally degraded with sufficient irradiation time. With the analysis of the intermediates in the photocatalytic degradation process of TTCH, the photocatalytic TTCH degradation pathway was proposed and is shown in Fig. 9.

Based on the above results, the mechanism of photocatalytic TTCH degradation by BOB-S nanosheets under visible light irradiation was elucidated and is shown in Fig. 10. First, because of the narrow band gap of 2.30 eV, BOB-S was excited by visible light irradiation and the h^+-e^- pairs were separated. Then, the photogenerated e^- was transferred to CB and trapped by the bromine vacancies on the surface or in the shallow lattice, resulting in a high-efficiency separation of the h^+-e^- pairs. After that, free radicals including $^\bullet O_2^-$ and $^\bullet$OH were generated by BOB-S and transformed, which were responsible for the TTCH degradation. Finally, TTCH was excited by $^\bullet$OH and degraded into several types of intermediates and products by h^+ and $^\bullet$OH. This mechanism was also appropriate to describe the TTCH degradation by BOB-M and BOB-L, which exhibited a lower photocatalytic TTCH degradation activity.

4. Conclusions

In this work, a series of $Bi_{24}O_{31}Br_{10}$ nanosheets with different thickness were successfully synthesized using a simple solvothermal method for the first time, and no surfactants were used in this synthetic process. The charge carrier density and the charge transfer efficiency were higher when the nanosheet thickness shifted from thin to ultrathin, which was ascribed to the increased ratio of the bromine vacancies on the surface or in the shallow lattice. The ultrathin $Bi_{24}O_{31}Br_{10}$ nanosheets exhibited the best performance for TTCH degradation under visible light irradiation. The TTCH degradation mechanism by the as-prepared BOB-S nanosheets under visible light irradiation was elucidated, and the degradation of TTCH greatly relied on the generated free radicals and the photogenerated h^+, which were formed by the photogenerated charge carriers. Our findings show promising applications of the bismuth oxybromide photocatalysts in water and wastewater treatment, and provide a new strategy for nano-scale photocatalyst design.

Acknowledgments

We thank the National Science Foundation of China (21261160489, 21590812 and 51538011) and the Collaborative Innovation Center of Suzhou Nano Science and Technology of the Ministry of Education of China for support of this work.

Appendix A. Supplementary data

Supplementary data associated with this article can be found, in the online version, at http://dx.doi.org/10.1016/j.apcatb.2017.01.015.

References

[1] I. Chopra, M. Roberts, Microbiol. Mol. Biol. Rev. 65 (2001) 232–260.
[2] Y. Ma, N. Gao, C. Li, Environ. Eng. Sci. 29 (2012) 357–362.
[3] Y. Shi, Z. Yang, B. Wang, H. An, Z. Chen, H. Cui, Appl. Clay Sci. 119 (2016) 311–320.
[4] Z. Li, L. Zhu, W. Wu, S. Wang, L. Qiang, Appl. Catal. B: Environ. 192 (2016) 277–285.
[5] S. Ma, J. Xue, Y. Zhou, Z. Zhang, RSC Adv. 5 (2015) 40000–40006.
[6] X. Xiao, R. Hu, C. Liu, C. Xing, X. Zuo, J. Nan, L. Wang, Chem. Eng. J. 225 (2013) 790–797.
[7] J. Li, Y. Yu, L. Zhang, Nanoscale 6 (2014) 8473–8488.
[8] L. Zhang, Y. Zhu, Catal. Sci. Technol. 2 (2012) 694–706.
[9] K. Li, Y. Tang, Y. Xu, Y. Wang, Y. Huo, H. Li, J. Jia, Appl. Catal. B: Environ. 140–141 (2013) 179–188.
[10] J. Zhu, S. Wang, J. Wang, D. Zhang, H. Li, Appl. Catal. B: Environ. 102 (2011) 120–125.
[11] H. Park, H.I. Kim, G.H. Moon, W. Choi, Energy Environ. Sci. 9 (2016) 411–433.
[12] X. Van Doorslaer, P.M. Heynderickx, K. Demeestere, K. Debevere, H. Van Langenhove, J. Dewulf, Appl. Catal. B: Environ. 111–112 (2012) 150–156.
[13] Y. Liu, A. Tang, Q. Zhang, Y. Yin, J. Am. Chem. Soc. 137 (2015) 11327–11339.
[14] Y. Wang, R. Shi, J. Lin, Y. Zhu, Energy Environ. Sci. 4 (2011) 2922.
[15] F. Xu, Y. Shen, L. Sun, H. Zeng, Y. Lu, Nanoscale 3 (2011) 5020.
[16] J. Jiang, K. Zhao, X. Xiao, L. Zhang, J. Am. Chem. Soc. 134 (2012) 4473–4476.
[17] H. Li, J. Shang, Z. Ai, L. Zhang, J. Am. Chem. Soc. 137 (2015) 6393–6399.
[18] W.K. Wang, J.J. Chen, M. Gao, Y.X. Huang, X. Zhang, H.Q. Yu, Appl. Catal. B: Environ. 195 (2016) 69–76.
[19] J. Tao, T. Luttrell, M. Batzill, Nat. Chem. 3 (2011) 296–300.
[20] J. Li, K. Zhao, Y. Yu, L. Zhang, Adv. Funct. Mater. 25 (2015) 2189–2201.
[21] J. Bao, X. Zhang, B. Fan, J. Zhang, M. Zhou, W. Yang, X. Hu, H. Wang, B. Pan, Y. Xie, Angew. Chem. 54 (2015) 7399–7404.
[22] A.M. Ganose, M. Cuff, K.T. Butler, A. Walsh, D.O. Scanlon, Chem. Mater. 28 (2016) 1980–1984.
[23] Y. Ao, K. Wang, P. Wang, C. Wang, J. Hou, Appl. Catal. B: Environ. 194 (2016) 157–168.
[24] J. Li, S. Sun, C. Qian, L. He, K.K. Chen, T. Zhang, Z. Chen, M. Ye, Chem. Eng. J. 297 (2016) 139–147.
[25] J. Di, J. Xia, M. Ji, B. Wang, S. Yin, Q. Zhang, Z. Chen, H. Li, Appl. Catal. B: Environ. 183 (2016) 254–262.
[26] X. Xiong, L. Ding, Q. Wang, Y. Li, Q. Jiang, J. Hu, Appl. Catal. B: Environ. 188 (2016) 283–291.
[27] D. Wu, S. Yue, W. Wang, T. An, G. Li, H.Y. Yip, H. Zhao, P.K. Wong, Appl. Catal. B: Environ. 192 (2016) 35–45.

[28] F.T. Li, Q. Wang, J. Ran, Y.J. Hao, X.J. Wang, D. Zhao, S.Z. Qiao, Nanoscale 7 (2015) 1116–1126.
[29] Z. Liu, J. Liu, Z. Liu, J. Niu, P. Feng, Mater. Res. Bull. 81 (2016) 119–126.
[30] Z. Liu, J. Niu, P. Feng, Y. Zhu, Ceram. Int. 41 (2015) 4608–4615.
[31] Y. Peng, P.-P. Yu, Q.-G. Chen, H.-Y. Zhou, A.-W. Xu, J. Phy. Chem. C 119 (2015) 13032–13040.
[32] L. Ye, X. Jin, C. Liu, C. Ding, H. Xie, K.H. Chu, P.K. Wong, Appl. Catal. B: Environ. 187 (2016) 281–290.
[33] M. Guan, C. Xiao, J. Zhang, S. Fan, R. An, Q. Cheng, J. Xie, M. Zhou, B. Ye, Y. Xie, J. Am. Chem. Soc. 135 (2013) 10411–10417.
[34] L. Ye, X. Jin, Y. Leng, Y. Su, H. Xie, C. Liu, J. Power Sources 293 (2015) 409–415.
[35] C.Y. Wang, X. Zhang, H.B. Qiu, W.K. Wang, G.X. Huang, J. Jiang, H.Q. Yu, Appl. Catal. B: Environ. 200 (2017) 659–665.
[36] L. Ye, Y. Su, X. Jin, H. Xie, C. Zhang, Environ. Sci.: Nano 1 (2014) 90–112.
[37] C.Y. Wang, X. Zhang, X.N. Song, W.K. Wang, H.Q. Yu, ACS Appl. Mater. Interfaces 8 (2016) 5320–5326.
[38] D.C. Hurum, A.G. Agrios, K.A. Gray, T. Rajh, M.C. Thurnauer, J. Phys. Chem. B 107 (2003) 4545–4549.
[39] M. Pan, H. Zhang, G. Gao, L. Liu, W. Chen, Environ. Sci. Technol. 49 (2015) 6240–6248.
[40] X. Xiao, J. Jiang, L. Zhang, Appl. Catal. B: Environ. 142–143 (2013) 487–493.
[41] H. Li, L. Zhang, Nanoscale 6 (2014) 7805–7810.
[42] H. Huang, X. Han, X. Li, S. Wang, P.K. Chu, Y. Zhang, ACS Appl. Mater. Interfaces 7 (2015) 482–492.
[43] L. Yu, X. Zhang, G. Li, Y. Cao, Y. Shao, D. Li, Appl. Catal. B: Environ. 187 (2016) 301–309.